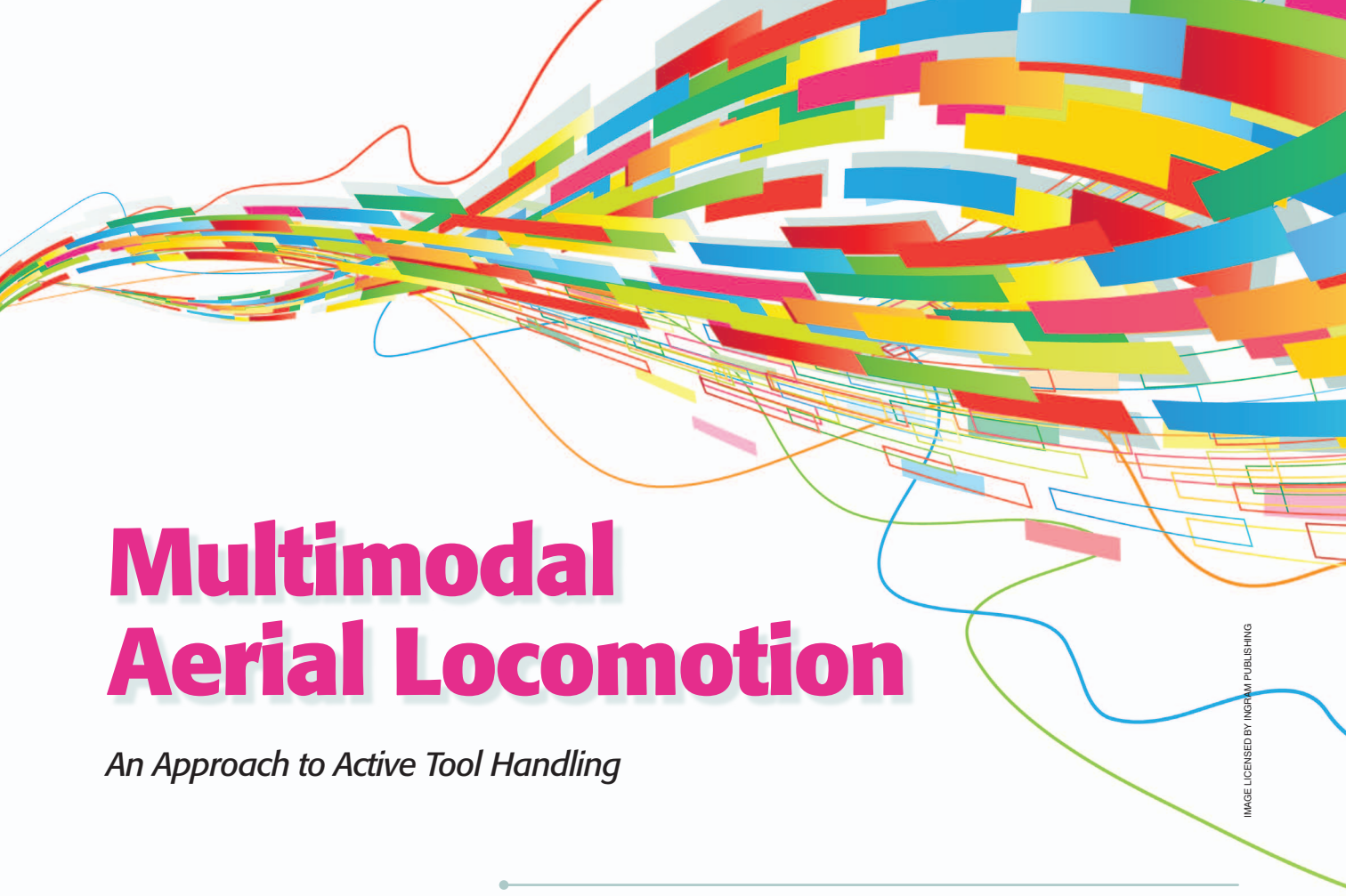

Multimodal Aerial Locomotion

An Approach to Active Tool Handling

By Han W. Wopereis, Wilbert L.W. van de Ridder, Tom J.W. Lankhorst, Lucian Klooster, Evyatar M. Bukai, David Wuthier, George Nikolakopoulos, Stefano Stramigioli, Johan B.C. Engelen, and Matteo Fumagalli

The research focus in aerial robotics is shifting from contactless inspection toward interaction and manipulation, with the number of potential applications rapidly increasing [1]. Eventually, aerial manipulators, i.e., unmanned aerial vehicles (UAVs) equipped with manipulators, will likely take on hazardous maintenance tasks now performed by humans. For this to happen, aerial manipulators must be able to perform all the different operations required in these maintenance routines.

Many such operations demand that the aerial manipulator either move or position a tool precisely on the surface of a static object, while generating sufficient contact force on the tool for correct operation. Examples of such operations are cleaning, grinding, and taking measurements. These operations present two main challenges:

1) They require the contact forces to be sufficiently large and persistent to perform meaningful operations on the surface.
2) They require that the tool can be moved over the surface on which the operation takes place.

Digital Object Identifier 10.1109/MRA.2018.2869527
Date of publication: 12 October 2018

These challenges are even more problematic when the aerial platform is underactuated, as is the case for the vast majority of commercially available aerial platforms. For this class of UAVs, contact constraints alter the dynamics in interaction, thus introducing additional coupling terms between the linear and rotational dynamics [2]. These constraints, in combination with the anisotropy of the torque limits, complicate the task of both applying relevant contact force and moving the tool on the surface.

Regular multirotors—multirotors with coplanar rotors—typically use classical control approaches to maintain stability up to certain interaction forces [3] (the boundaries for stability are assessed in [4]). This approach has been adopted in [5] to apply a quadrotor as a three-dimensional (3-D) force effector. Typically, in scenarios that require substantial interaction forces, contacts placed widely apart are used to constrain the rotational dynamics, while contact force is generated by additional rotors [6], tilting rotors [7], or full-body rotation [8]. However, the use of widely spaced contacts restricts the system's motion capabilities.

Instead of regular multirotors, fully actuated multirotors can be used as the floating base platform for the aerial manipulator, because these do not suffer from the intrinsic

challenges posed by underactuation [9]. In this case, rotors can be placed in different noncoplanar configurations [9], [10], or mechanisms can be designed that adjust the orientation of the rotors with respect to the frame fixed to the body [11]. However, these systems have different drawbacks: they require additional mechanisms, adding weight to the system, and they use noncoplanar configurations, which means some rotors may not fully contribute to the generated output thrust.

Rarely has a UAV been shown to successfully operate a tool upon the surface of a static object. Such UAV-driven approaches, however, while applying only limited interaction forces, have demonstrated that active movement over a surface is possible [12], [13].

In this article, we introduce, as an alternative to UAV-driven locomotion, the concept of multimodal aerial locomotion for active tool handling in aerial manipulation (Figure 1). Demonstrations have shown that multimodal locomotion can provide additional locomotion capabilities in situations where a single modality would be insufficient to accomplish the task [14], [15]. We present a novel platform that exploits two locomotion modalities to achieve precise tool positioning and persistent contact force. To create this platform, we combined an aerial manipulator with a wheeled end effector. Three actuated omnidirectional wheels were placed on this end effector to allow active locomotion of the tool, which required sufficient friction with the surface to function correctly. To guarantee this friction, a controller based on our previous work [2] was applied. The scope of this controller is twofold: 1) it provides the contact force necessary to ensure wheeled locomotion and tool operation, and 2) it stabilizes the attitude of the UAV subject to the interaction forces.

We evaluated the approach in experiments in which the end effector, with a cleaning brush attached, is used to clean off a drawing made by a marker on a flat vertical surface. The results of these experiments demonstrate effective locomotion of both the aerial and wheeled systems, thus validating our approach to multimodal locomotion for active tool handling.

Multimodal Aerial Locomotion Approach

The main task attempted in the experiments described in this article resembles a maintenance operation on a wind turbine—the cleaning of a confined region on its static surface. To demonstrate the multimodal locomotion approach, we considered a challenging scenario: moving an end effector on a vertical surface. For the sake of simplicity but in keeping with the general requirements of related tasks, we used a flat rigid surface and assumed knowledge of the position and orientation of the surface at the region of interest.

Within this scenario, our multimodal locomotion approach for performing the required surface operation task used an aerial manipulator with an end effector, on which the brushing tool was mounted along with wheels that allowed for active repositioning on the surface. This is sketched in Figure 2.

The multimodal locomotion system consists of a regular multirotor, a 1-degree-of-freedom (DoF) manipulator, and a custom-designed end effector. The multirotor constitutes the aerial-locomotion system, which we define as a system that is not constrained to a static environment. The multirotor functions as the base for the manipulator. On one extremity, the manipulator contains a 1-DoF joint, which connects to the multirotor and decouples the pitch of the multirotor. On the other extremity, a flexible joint connects the manipulator and the end effector, decoupling their relative orientation. The end effector, by means of an omnidirectional driving unit, performs the ground locomotion, which we define as the locomotion on a static environment. This design enables the operator to reposition the tool and control its operation.

The symbiosis between the aerial-locomotion system and the ground-locomotion system is the key element that allows the task to be accomplished. The aerial-locomotion system carries the tool to the desired location, while accuracy in positioning the tool is achieved by the ground-locomotion system. A normal force between the surface and the wheels is required to generate friction for the ground-locomotion system to work. To clean a vertical surface, this normal force can be achieved only by the aerial system pushing the ground-locomotion system onto the surface.

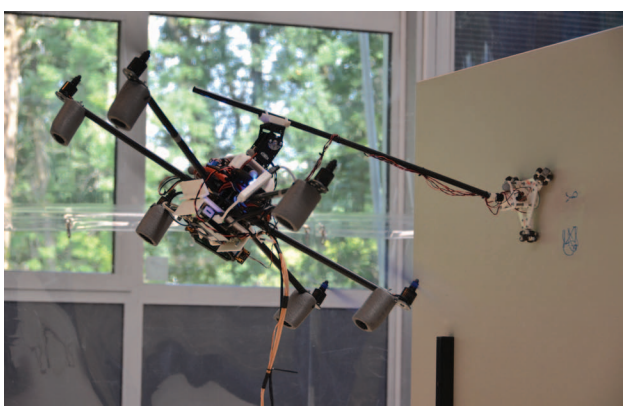

Figure 1. A photo demonstrating the multimodal locomotion system performing a cleaning operation on a vertical surface.

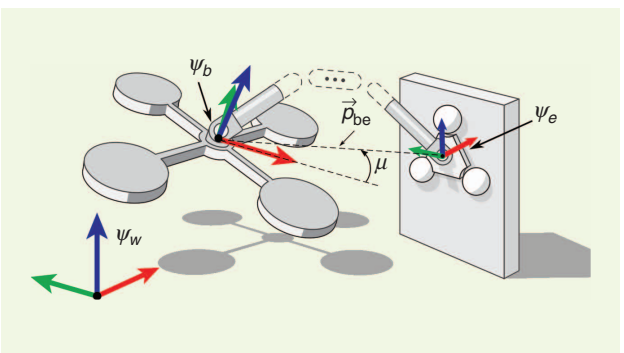

Figure 2. An illustration of the aerial manipulator showing the inertial (world) frame Ψ_w, the body-fixed frame of the multirotor Ψ_b, and the end-effector frame Ψ_e. The red, green, and blue axes represent $(\hat{x}, \hat{y}, \hat{z})$, respectively.

As a consequence of coupling the aerial-locomotion system to the ground-locomotion system, we must ensure that displacements of the ground-locomotion system do not affect the stability of the aerial-locomotion system. Due to the presence of constraints, movements of the ground-locomotion system affect the dynamic behavior of the aerial system. This introduces disturbances in the form of forces applied to the tip of the manipulator, which results in a rotation and displacement of the aerial system. To deal with this undesired effect, we used a modified controller based on our previous work [2]. This contact controller stabilizes the relative orientation of the multirotor to the end effector, thus offsetting the effects of disturbances caused by the coupling with the end effector. This stabilization results in automatic tracking of the ground locomotion.

In practice, this implies that any time the motion of the end effector disturbs the multirotor, the multirotor will respond by stabilizing itself in a new equilibrium position. This self-stabilization allows us to control the position of the multirotor implicitly by controlling the position of the ground-locomotion system. An elastic element provides the rotational decoupling necessary to facilitate this effect. The rotational compliance introduces a spherical constraint that allows relative displacements between the multirotor and the end effector. This is needed to allow the contact controller to react to the displacement within its bandwidth. Besides stabilizing the system, the contact controller serves the task of providing the normal forces required for successful ground locomotion and tool operation.

End-Effector Design

The end effector, which is detailed in Figure 3, was designed to move along the surface and perform surface operations (in this case brushing). Both these functions require a normal force to be applied to the end effector. Therefore, in crafting the end effector, designers place special emphasis on making it robust yet lightweight.

The body of the end effector was formed by the base and top platforms, which were rigidly connected by three metal spacers. To enable the end effector to move along the surface, three actuated omnidirectional wheels were attached to the base platform at 120° angles. Each of these wheels was actuated in one direction and contained freely rotating barrels that allowed movement in the other direction. This combination of three independently driven wheels resulted in full controllability of the end effector's pose on the surface, assuming sufficient friction.

The brushing system, as detailed in the bottom part of Figure 3, represented the surface operation functionality. It is possible to use different types and sizes of tools, which may require different surface pressure, depending on the operation. To control this surface pressure, the tool was mounted on a parallel structure suspended by three compression springs. The parallel structure comprised three hinge beams connecting the motor mount to linear slider bearings, which slid over the linear guides. These linear guides are, in fact, the spacers between the top and bottom platforms. The beams' material stiffness allowed minor rotational misalignment of the tool. In the uncompressed state, the springs press the brushing system against the base platform so that the brush sticks out. When compressed, with all wheels in contact with the surface, the springs apply a constant force on the brushing system that is independent of the drone's contact force.

The prototype of the end effector (Figure 4) weighed 0.15 kg and carried a flat, soft brush having a diameter of 3 cm. The suspension was designed to apply a force of 6 N in the compressed state, which translates to an applied pressure of 8,500 Pa. Four high-power 300:1 Pololu Micro Metal gearmotors were used to actuate the wheels and the brush, both controlled by an Adafruit Feather board. Open-loop control was applied for the ground locomotion, with Cartesian body-velocity commands ranging from $[-1, 1]$ as input. The flexible joint connecting the end effector and the manipulator was implemented as a male-to-male M5 rubber shock mount with a compression load of 200 N, shown in the top part of Figure 4.

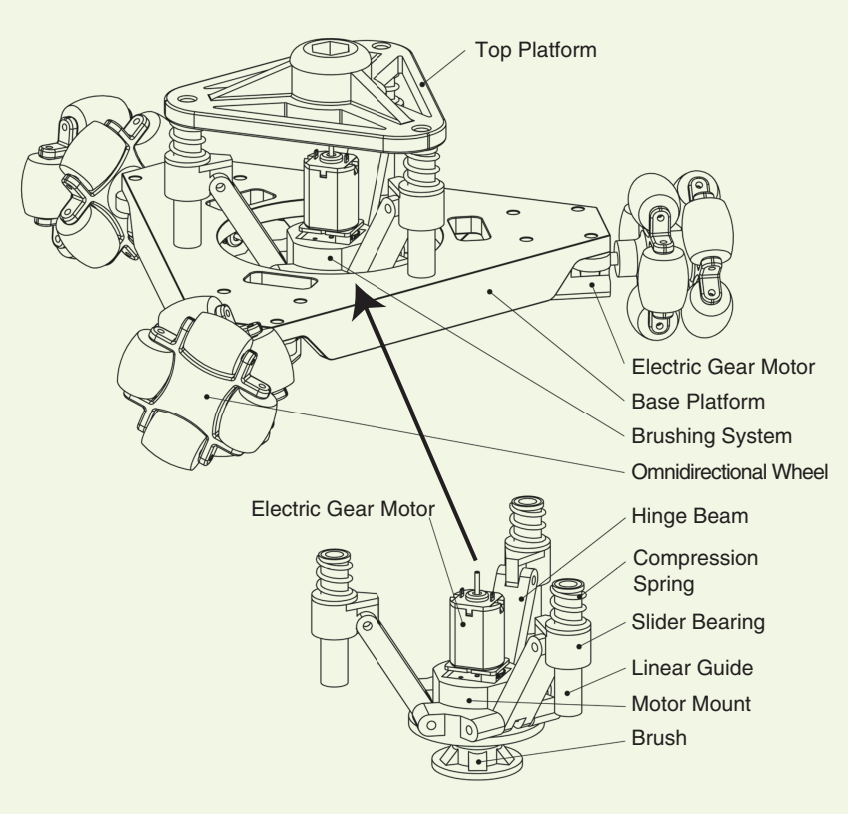

Figure 3. An illustration of the end-effector design.

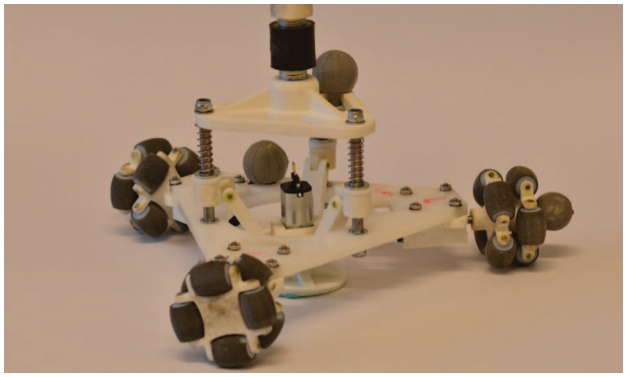

Figure 4. The end-effector prototype. Except for the metal components, motor, and flexible element, all parts were produced using rapid-prototyping techniques.

Control Strategy

We define the frames in our system as illustrated in Figure 2. Frames Ψ_w, Ψ_b, and Ψ_e represent the inertial (world) frame, the multirotor's body-fixed frame, and the end-effector frame, respectively. Frame Ψ_b has its origin in the center of mass of the multirotor, with $\hat{x}_b$ aligned with the forward direction and $\hat{z}_b$ with the thrust vector. Frame Ψ_e is oriented as Ψ_w and has its origin in the elastic component connecting the end effector to the manipulator. The roll, pitch, and yaw angles of the multirotor around $(\hat{x}_b, \hat{y}_b, \hat{z}_b)$ are denoted by $(\phi_b, \theta_b, \psi_b)$, respectively. We assume that the origin of frame Ψ_e, p_e always lies in the $(\hat{x}_b, \hat{z}_b)$ plane. This implies that the pitch angle and thrust of the multirotor define the magnitude of the contact force. The manipulator angle μ is given by the angle between the axis $\hat{x}_b$ and the vector $\vec{p}_{be}$ expressed in Ψ_b, and positive rotation is defined counterclockwise with respect to $\hat{y}_b$. We assume a constant distance between Ψ_b and Ψ_e, annotated by L_m.

Considering our application scenario, four phases for the system can be identified: free flight, engage, contact, and disengage. The engage phase is the period during which the approach is initiated up until the system is in stable contact. The disengage phase occurs from the moment the separation is initiated until the system has recovered its position set-point, placed at a fixed distance C from the surface. At the start of the engage phase, we require that the end effector be near the surface (<30 cm).

Figure 5 illustrates the switching control strategy used during the different phases. Two separate controllers are used: a free-flight controller and a contact controller. Depending on the phase, different inputs are given to these controllers, and different controller outputs are used. The same applies for the manipulator set-point. Both controllers receive the multirotor's state information: position p_b, velocity v_b, orientation R_b^w, and angular rates ω_b.

As Figure 5 shows, the free-flight controller is used with the manual set-points in the free-flight phase; during the disengage phase, the controller has a constant set-point C from the surface, determined at the start of the disengage phase. In the engage phase, the implementation of the contact controller as presented in [2] is used, with the three desired body angles as reference inputs and the height set-point given by $z_{sp} = z_b(t_e)$, where t_e is the time the engage mode was entered. During the contact phase, the modified implementation of the contact controller, as described in the following, is used so that the controller depends only on angular set-points and angular state measurements. This controller is position-independent, which allows the multirotor to track the ground locomotion without active coordination between the set-points of the end effector and the multirotor.

Because a vertical surface is assumed, the manipulator is given the set-point $\mu_{sp} = \theta_b$ in the free-flight, engage and disengage phases, so that the end effector is always in front of Ψ_b. The manipulator is assumed sufficiently fast to accurately track θ_b. In the contact phase, the manipulator set-point is set to a specified value $\mu_{sp} = \mu_c$, which follows from the conditions required for equilibrium.

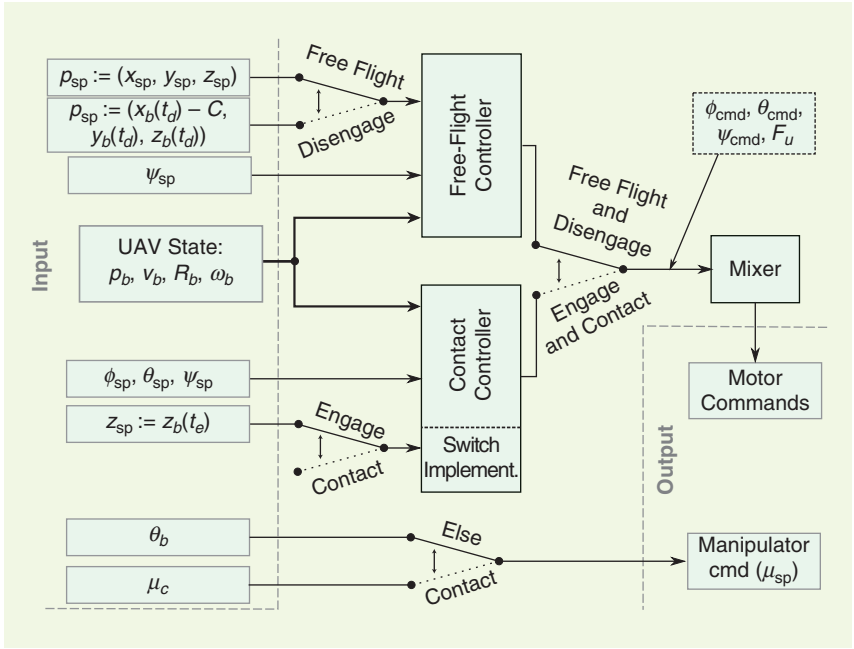

Figure 5. A schematic illustrating the switching control strategy. Depending on the phase, different inputs and outputs are selected.

Control Algorithms

Free-Flight Controller

The free-flight controller in the experiments described here consisted of a generic cascaded position controller. It consists of four different stages, where each subsequent stage takes the output of the previous stage

as the reference input. In order, these controllers are a proportional controller on the position, velocity, and attitude errors and a proportional–integral–derivative controller on the angular rate error. Due to the cascaded structure, subsequent control stages acted as damping on the previous stages. Additional integral and derivative actions were added to the rate-control loop to increase the tracking performance of the angular rates.

Furthermore, gravity compensation was taken into account, and a static center-of-mass correction was applied. The latter was required because the additional weight of the manipulator and end effector affected the center of mass of the total system. Given the structure of the manipulator we used, the variations in the center of mass were considered negligible. As such, the center-of-mass correction yielded a constant compensation torque about $\hat{y}_b$. The value was found empirically by readjusting the compensation torque until the set-point and actual position in free flight match.

Contact Controller

The contact controller, based on the work presented in [2], is specifically designed for use when the system is in contact with the environment. We demonstrated that stability in the contact phase can be maintained while simultaneously applying a substantial contact force. This result was achieved by actively exploiting the coupling between the roll and yaw state during the contact phase, while retaining the regular controllers for the pitch and altitude. For this article, a modified version of the controller presented in [2] was derived specifically for the contact phase. This version of the controller relies solely on angular state measurements to maintain its orientation relative to the end effector and is therefore fully position independent. This allows the multirotor to automatically track end effector movements without requiring active adjustments to its set-points.

In this derivation, we considered the end effector to be fixed to the surface due to friction and normal force. Meanwhile, we considered the manipulator to be connected to the end effector by a spherical joint in Ψ_e. Furthermore, we assumed that the static vertical surface is oriented so that $\hat{x}_e$ is perpendicular to it and points inwards. Applying screw theory [16] and ignoring frictional effects, the equations of motion expressed in Ψ_b can be described as follows:

$$I_b \dot{T}_b^{b,e} = \mathrm{ad}^{\mathrm{T}}_{T_b^{b,e}} I_b T_b^{b,e} + \mathrm{Ad}^{\mathrm{T}}_{H_b^g}(W_g)^{\mathrm{T}} + (W_b)^{\mathrm{T}} + \mathrm{Ad}^{\mathrm{T}}_{H_b^e}(W_e)^{\mathrm{T}}. \tag{1}$$

Here, $I_b \dot{T}_b^{b,e}$ is the change in momentum of the multirotor with respect to Ψ_e, with I_b representing the inertia of the multirotor and $T_b^{b,e}$ the relative twist of Ψ_b to Ψ_e expressed in Ψ_b. The fictitious forces are accounted for by $\mathrm{ad}^{\mathrm{T}}_{T_b^{b,e}} I_b T_b^{b,e}$ (Ψ_b is not an inertial frame). W_g, W_b, and W_e are the gravity, input, and contact wrenches, respectively. $H_i^j \in SE(3)$ is the homogeneous transformation matrix from Ψ_i to Ψ_j. The matrix $\mathrm{Ad}^{\mathrm{T}}_{H_i^j}$ describes the transformation of a given wrench from frame j to frame i. Ψ_g is the gravitational frame, which coincides with Ψ_b and is oriented as Ψ_w. Note that H_b^e depends on μ_{sp} and L_m.

Assuming quasistatic conditions, the reaction wrench of the environment can be found using the balance of forces:

$$(W_e)^T = \begin{bmatrix} 0^{3\times 1} \\ -R_b^e \begin{bmatrix} 0 \\ 0 \\ F_u \end{bmatrix} + \begin{bmatrix} 0 \\ 0 \\ m_u g \end{bmatrix} \end{bmatrix}, \tag{2}$$

where F_u and m_u are the thrust and mass of the multirotor, respectively. Because I_b is invertible, by combining and rearranging (1) and (2), the dynamics of the constrained system can be described as

$$\dot{T}_b^{b,e} = f(T_b^{b,e}, H_b^e, U, \mu_{\mathrm{sp}}), \tag{3}$$

with $U := [\tau_x, \tau_y, \tau_z, F_u]^T$ being the input torques and thrust generated by the multirotor.

Due to the constraints imposed on the system, the multirotor can be stabilized by stabilizing its rotational dynamics. For this, we used a state-feedback controller. To apply such a controller, (3) is linearized around the equilibrium state given by the following:

$$\begin{aligned} &\phi_b = 0; \quad \dot{\phi}_b = 0; \quad \theta_b = \theta_{\mathrm{sp}}; \\ &\dot{\theta}_b = 0; \quad \psi_b = 0; \quad \dot{\psi}_b = 0; \\ &\tau_{x,y,z} = 0; \quad F_u = F_{\mathrm{eq}}; \quad \mu_c = \theta_{\mathrm{sp}}, \end{aligned} \tag{4}$$

where the pitch set-point θ_{sp} is given as an input and F_{eq} is the thrust needed for the system to remain in equilibrium, given by the following:

$$F_{\mathrm{eq}} = \frac{m_u g}{\cos(\theta_{\mathrm{sp}})}. \tag{5}$$

Note that, in the equilibrium configuration, the reader could estimate the normal force F_N applied by the system on the environment by using the following relation:

$$F_N = \frac{m_u g}{\tan(\theta_{\mathrm{sp}})}. \tag{6}$$

We represent the linearized rotational dynamics as follows:

$$\dot{X} = A(\theta_{\mathrm{sp}})(X - X_{\mathrm{eq}}) + B(\theta_{\mathrm{sp}})(U - U_{\mathrm{eq}}), \tag{7}$$

with $X = [\phi_b \;\; \dot{\phi}_b \;\; \theta_b \;\; \dot{\theta}_b \;\; \psi_b \;\; \dot{\psi}_b]^T$ describing the angular state. X_{eq} and U_{eq} are filled with the equilibrium values of (4).

The linear quadratic regulator method, combined with gain-scheduling, can be applied to (7) to find stabilizing control gains $K(\theta_{\mathrm{sp}})$ for each θ_{sp} so that

$$U = K(\theta_{\mathrm{sp}})(X_{\mathrm{sp}} - X) + U_{\mathrm{eq}} \tag{8}$$

stabilizes the rotational dynamics of the system. This results in gain matrices of the following shape:

$$K = \begin{bmatrix} K_{1,1} & K_{1,2} & 0 & 0 & K_{1,5} & K_{1,6} \\ 0 & 0 & K_{2,3} & K_{2,4} & 0 & 0 \\ K_{3,1} & K_{3,2} & 0 & 0 & K_{3,5} & K_{3,6} \\ 0 & 0 & K_{4,3} & K_{4,4} & 0 & 0 \end{bmatrix}, \quad (9)$$

which indicate a distinct separation between the roll and yaw states, stabilized using the roll torque and yaw torque, and the pitch state, stabilized by the pitch torque and the variation in thrust.

Experiments

Experiments were performed to evaluate the multimodal approach toward surface cleaning (presented in the "Multimodal Aerial Locomotion Approach" section) and the control strategy (presented in the "Control Strategy" section), which are reported here. We have included a supplementary multimedia file showing the experiments. This is available at http://ieeexplore.ieee.org.

Experimental Setup

The experimental setup consisted of an aerial manipulator, a ground-control station, an Optitrack motion capture system, and a vertical surface. As shown in Figure 1, the aerial manipulator comprises a hexarotor platform equipped with a single actuator manipulator, which carries the end effector presented in the section "End-Effector Design." The system was controlled by an onboard Intel NUC i5 computer that communicates with the ground-control station over a wireless network. The ground-control station provided the user interface to the operator. The motion capture system obtained absolute pose measurements, which were used for the multirotor's state estimation algorithm and to obtain experimental measurement results.

The hexarotor we used is illustrated in Figure 1. Its diameter (excluding propellers) is 80 cm, and it weighs 2.1 kg. A frame with long arms was chosen deliberately to increase the gap between the front propellers and thus allow the manipulator to pass through. The hexarotor was controlled by a Pixhawk 2.1 flight controller, running PX4 Firmware [17]. Its propulsion system consisted of Cobra ESC CM2217 950-Kv motors and 10×4.5-in dual-blade propellers. The aerial system was powered by a tethered 16-V power supply. At this voltage, the configuration can provide a maximum F_u of 78 N.

The manipulator consisted of a Dynamixel MX106R servo motor, which rotates along $\hat{y}_b$, and a hollow carbon-fiber tube connected on top of this servo. The tube had a length of 60 cm, an inner diameter of 10.5 mm, and an outer diameter of 12 mm, which provided a sufficient stiffness for us to assume negligible deflection of the tube, given the weight of the end effector. At the end of this rod, a 3-D-printed bend is attached that applies an angular correction because the rod is not exactly aligned with the vector $\vec{p}_{be}$. This bend connects to the elastic component of the end effector. The manipulator weighs 0.23 kg.

Experiment Description

Two sets of experiments were conducted in a confined flying arena where a wall was placed at $x_w = 1.6$ m in the first set of experiments and $x_w = 1.75$ m in the second set. In both cases, the wall was aligned with the plane $(\hat{y}_w, \hat{z}_w)$ such that, in interaction, Ψ_w and Ψ_e have identical orientations.

In the first set of experiments the goal was to clean a scribble from the wall. This scribble was drawn on a patch measuring 5 cm wide and 10 cm high on the wall. An operator controlled p_{sp} during the free-flight and engage phases and θ_{sp} during the engage and contact phases. To establish quick and reliable contact, θ_{sp} was set to 20° before entering the engage phase. Regarding the end effector, the operator activated the brush and controlled the lateral movement by giving lateral velocity commands. The operator initiated the engage, contact, and disengage phases in the experiment. The disengage distance C was set to 0.75 m.

In the second set of experiments, the repeatability of the approach was qualitatively evaluated. The switching control procedure was automated and repeated for several runs, each lasting 64 s. This procedure was as follows. First, the surface was approached by incremental adjustments of the p_{sp} in the free-flight phase. Then, the engage phase was initiated. Rather than using an immediate 20° set-point, θ_{sp} was gradually increased from 12° to 20° over a period of 4 s to reduce the shock of impact. Then, the contact phase was initiated, and θ_{sp} was gradually increased further to 27°. An up-down locomotion was performed by sending a velocity command of 0.125 in both directions for 6 s, with a pause of 2 s in between, after which the disengage phase was initiated.

Results

In the first set of experiments, several trials were performed under contact angles varying between 25° and 40° to qualitatively evaluate the performance and reliability of the system in interaction. In all of the experiments, the operator was able to remove the scribbles on the wall by controlling the ground locomotion.

The results of one trial of the first set are displayed in Figures 6, 7, and 8. Figure 6 shows the spatial position of the end effector during the experiment; a part of the surface is illustrated for clarity. In Figure 7, the pose of the multirotor and the μ_{sp} are plotted. Figure 8 shows the position and velocity commands of the end effector. The start of different events are annotated in Figures 6 and 7.

The experiment started with the system lifting off at $t = 10$ s and ascending to approximately 1 m. A small steady-state error between z_b and z_{sp} was visible due to a small error in estimating the system's mass and the lack of integral action in the altitude control loop. The multirotor was moved toward the surface, and at $t = 57.4$ s the operator started the engage phase: the system pitched forward and successfully established contact. Before contact with the surface was made, a small drop in height occurred, caused by the end-effector mass not being taken into account in the contact controller. This drop caused a mismatch between

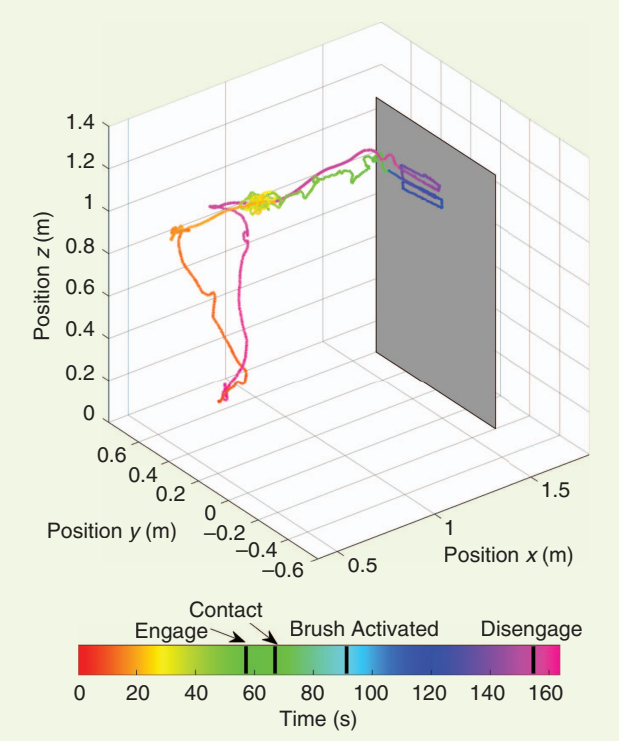

Figure 6. The end-effector position over time in a surface-cleaning experiment. Note that the end effector is positioned on a single point from $t \approx 60$ s to $t \approx 110$ s.

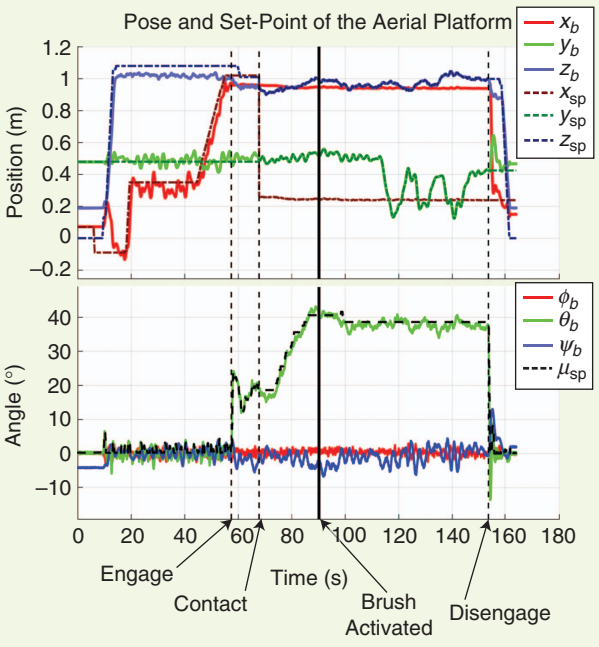

Figure 7. The pose of the multirotor and the angle of the manipulator plotted over time in the surface-cleaning experiment of Figure 6.

z_{sp} and z_e, which affected θ_b and resulted in temporary contact loss for the bottom wheel. In this experiment, the operator manually lowered z_{sp} to reduce this effect. After the system stabilized, the operator started the contact phase at $t = 67.8$ s.

During the contact phase, the controller depended entirely on angular measurements, and the position set-points were reinitialized to accommodate the disengage phase. The operator gradually increased θ_{sp} to the desired 40° and activated the brush at $t \approx 90.7$ s. From $t = 110$ s to $t = 150$ s, the operator actively controlled the locomotion of the ground system, moving it across the surface in the pattern illustrated in Figure 6, effectively cleaning the wall. In Figure 8, we observe that, when pure horizontal velocity commands are given, slight vertical displacements of the end effector also occur and vice versa. These displacements are caused by occasional slipping of individual wheels and by undesired rotations of the end effector on the surface. Although these displacements were seemingly small, the operator in several experiments had to compensate for them. After successfully cleaning the wall, the operator initiated the disengage phase at $t = 154$ s, returned the system to the free-flight phase, and safely landed it. We observe that, over the entire period in the contact, phase, ϕ_b and ψ_b never exceeded 7.5°.

One of the results of the second set of experiments is shown in Figure 9. In this experiment, 18 consecutive trials of the multimodal locomotion procedure were

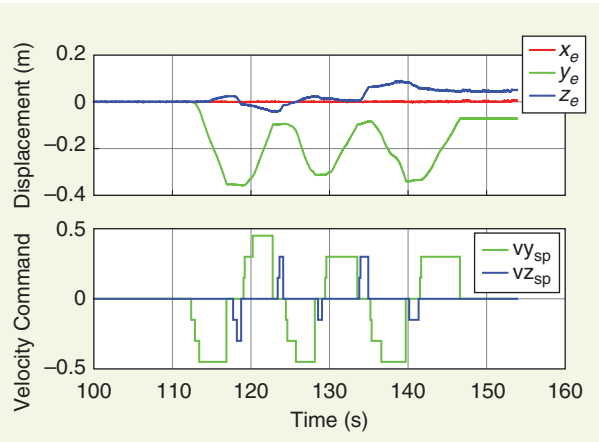

Figure 8. The relative displacement of the end effector and the associated velocity commands during the ground-locomotion phase in the experiment of Figure 6.

performed over 20 min. Figure 9(a) shows the surface motion trajectories of each trial. Except for trials 7 and 16, the motion profiles were quite similar. However, we noticed a sideways drift in the first point of attachment over the course of the experiment. We were unable to identify the cause of this drift. The controller effectively withstood disturbances and maintained stability in all 18 trials. In Figure 9(b), the orientation of the multirotor and the pose of the end effector are shown for trials 6, 7, 15, and 16. In trial 7, a coincidental bounce with the

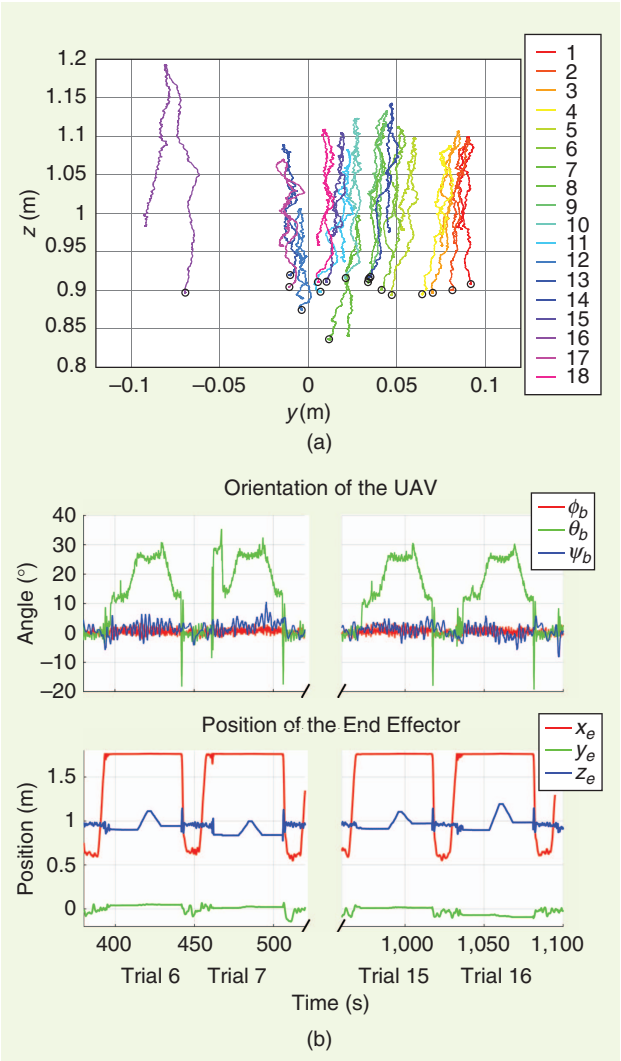

Figure 9. The results of the repeatability experiment in which 18 consecutive trials of the multimodal locomotion procedures were performed. The surface-movement trajectories are shown in (a). A trend can be noted in the point of attachment over time, which is indicated by the circles. In (b), the orientation of the multirotor and the position of the end effector is plotted for trials 6 and 7 and for trials 15 and 16.

environment occurred during approach (see x_e), which resulted in oscillations in θ_b, causing a vertical offset in the point of attachment (see z_e). From the video it appears that the horizontal offset in the 16th trial was caused by a bounce due to disturbances as well, in turn causing the system to make contact a bit farther to the side. We notice no remarkable behavior in the plots for trial 16.

Lessons Learned

From the experiments, several lessons were learned.

- Slipping of wheels occurred frequently, resulting in uncontrolled rotations of the end effector, which caused additional disturbances to the multirotor. The ground-locomotion system may benefit from a design with only two perpendicular actuated omnidirectional wheels, aligned such that slipping does not cause uncontrolled rotation. The rotation of the end effector on the surface may be controlled solely by the multirotor and the elastic element.
- Under certain relative orientations between the end effector and the multirotor, the elastic decoupling element applies undesired torque. This can cause disconnection of certain wheels, even if the net interaction force applied by the multirotor is properly aligned.
- The contact controller demonstrates resilience to the disconnection of individual wheels from the surface but becomes unstable whenever there is no contact with the environment, even for a brief moment. Therefore, persistence of contact is crucial, but persistent contact of all three wheels is not required.
- The contact controller outputs desired torque and thrust values. Given the importance of aligning the interaction force to the approach, it is crucial to have an accurate mapping from rotor thrust to rotor velocities. This mapping depends on voltage. Therefore, the use of batteries (e.g. in outdoor applications) may pose additional challenges.

Conclusions and Future Work

The multimodal locomotion system evaluated in this article is an approach to active tool handling in remote locations. The system was designed as an aerial manipulator carrying an end effector composed of three actuated omnidirectional wheels and a tool. The aerial manipulator represented the aerial-locomotion system, while the end effector represented the ground-locomotion system. The end effector was specifically designed to allow the repositioning of a tool on the surface. To deal with the issues related to the deployment this kind of platform, as described in the article, a control strategy based on the authors' previous work was modified and implemented on an experimental setup.

Experiments in which a 5×10-cm area was successfully cleaned with a 3-cm-diameter brush validated the approach. The results prove that the applied control strategy successfully counteracted the disturbances on the aerial platform introduced by the locomotion of the end effector, with the angular errors remaining below 7.5°. The repeatability of the multimodal locomotion approach was qualitatively demonstrated by an experiment in which 18 consecutive trials were stably performed.

The success of these experiments naturally suggests an extension of this approach to surfaces of any orientation and curvature so that a broader range of scenarios might be examined. Furthermore, strategies for trajectory generation can be investigated to seamlessly transition from free flight to contact with the environment. Finally, the switching nature of the proposed control strategy should be studied.

Acknowledgments

This work was funded by the European Commission's H2020 project AEROWORKS under Grant 644128. We thank G. te Riet o/g Scholten, V. Groenhuis, and S. Smits for their advice

and assistance in manufacturing the prototype and A. de Vries for his help in setting up the experimental space.

References

[1] F. Ruggiero, V. Lippiello, and A. Ollero, "Aerial manipulation: A literature review," *IEEE Robot. Automat. Lett.*, vol. 3, no. 3, pp. 1957–1964, 2018.

[2] H. W. Wopereis, J. J. Hoekstra, T. H. Post, G. A. Folkertsma, S. Stramigioli, and M. Fumagalli, "Application of substantial and sustained force to vertical surfaces using a quadrotor," in *Proc. 2017 IEEE Int. Conf. Robotics and Automation (ICRA)*, pp. 2704–2709.

[3] M. Fumagalli, R. Naldi, A. Macchelli, F. Forte, A. Q. Keemink, S. Stramigioli, R. Carloni, and L. Marconi, "Developing an aerial manipulator prototype: Physical interaction with the environment," *IEEE Robot. Automat. Mag.*, vol. 21, no. 3, pp. 41–50, 2014.

[4] M. Orsag, C. Korpela, S. Bogdan, and P. Oh, "Dexterous aerial robots—mobile manipulation using unmanned aerial systems," *IEEE Trans. Robot.*, vol. 33, no. 6, pp. 1453–1466, Dec. 2017.

[5] G. Gioioso, M. Ryll, D. Prattichizzo, H. H. Bülthoff, and A. Franchi, "Turning a near-hovering controlled quadrotor into a 3D force effector," in *Proc. 2014 IEEE Int. Conf. Robotics and Automation (ICRA)*, pp. 6278–6284.

[6] A. Albers, S. Trautmann, T. Howard, T. A. Nguyen, M. Frietsch, and C. Sauter, "Semi-autonomous flying robot for physical interaction with environment," in *Proc. 2010 IEEE Conf. Robotics Automation and Mechatronics (RAM)*, pp. 441–446.

[7] C. Papachristos, K. Alexis, and A. Tzes, "Technical activities execution with a tiltrotor UAS employing explicit model predictive control," *IFAC Proc. Volumes*, vol. 47, no. 3, pp. 11,036–11,042, 2014.

[8] H. Tsukagoshi, M. Watanabe, T. Hamada, D. Ashlih, and R. Iizuka, "Aerial manipulator with perching and door-opening capability," in *Proc. 2015 IEEE Int. Conf. Robotics and Automation (ICRA)*, pp. 4663–4668.

[9] M. Ryll, G. Muscio, F. Pierri, E. Cataldi, G. Antonelli, F. Caccavale, and A. Franchi, "6D physical interaction with a fully actuated aerial robot," in *Proc. 2017 IEEE Int. Conf. Robotics and Automation (ICRA)*, pp. 5190–5195.

[10] S. Park, J. Her, J. Kim, and D. Lee, "Design, modeling and control of omni-directional aerial robot," in *Proc. 2016 IEEE/RSJ Int. Conf. Intelligent Robots and Systems (IROS)*, pp. 1570–1575.

[11] H.-N. Nguyen, S. Park, and D. Lee, "Aerial tool operation system using quadrotors as rotating thrust generators," in *Proc. 2015 IEEE/RSJ Int. Conf. Intelligent Robots and Systems (IROS)*, pp. 1285–1291.

[12] J. L. Scholten, M. Fumagalli, S. Stramigioli, and R. Carloni, "Interaction control of an UAV endowed with a manipulator," in *Proc. 2013 IEEE Int. Conf. Robotics and Automation (ICRA)*, pp. 4910–4915.

[13] K. Alexis, G. Darivianakis, M. Burri, and R. Siegwart, "Aerial robotic contact-based inspection: Planning and control," *Autonomous Robots*, vol. 40, no. 4, pp. 631–655, 2016.

[14] L. Daler, S. Mintchev, C. Stefanini, and D. Floreano, "A bioinspired multi-modal flying and walking robot," *Bioinspiration & Biomimetics*, vol. 10, no. 1, 2015. doi: 10.1088/1748-3190/10/1/016005.

[15] Y. Mulgaonkar, B. Araki, J.-S. Koh, L. Guerrero-Bonilla, D. M. Aukes, A. Makineni, M. T. Tolley, D. Rus, R. J. Wood, and V. Kumar, "The flying monkey: A mesoscale robot that can run, fly, and grasp," in *Proc. 2016 IEEE Int. Conf. Robotics and Automation (ICRA)*, pp. 4672–4679.

[16] S. Stramigioli and H. Bruyninckx, "Geometry and screw theory for robotics," in *Proc. 2001 IEEE Int. Conf. Robotics and Automation*, pp. 5–33.

[17] L. Meier, D. Honegger, and M. Pollefeys, "Px4: A node-based multithreaded open source robotics framework for deeply embedded platforms," in *Proc. 2015 IEEE Int. Conf. Robotics and Automation (ICRA)*, pp. 6235–6240.

Han W. Wopereis, University of Twente, Faculty of Electrical Engineering, Mathematics, and Computer Science, Center for Telematics and Information Technology, The Netherlands. E-mail: h.w.wopereis@utwente.nl.

Wilbert L.W. van de Ridder, University of Twente, Faculty of Electrical Engineering, Mathematics, and Computer Science, Center for Telematics and Information Technology, The Netherlands. E-mail: l.w.vanderidder@utwente.nl.

Tom J.W. Lankhorst, University of Twente, Faculty of Electrical Engineering, Mathematics, and Computer Science, Center for Telematics and Information Technology, The Netherlands. E-mail: t.j.w.lankhorst@utwente.nl.

Lucian Klooster, University of Twente, Faculty of Electrical Engineering, Mathematics, and Computer Science, Center for Telematics and Information Technology, The Netherlands. E-mail: l.klooster@student.utwente.nl.

Evyatar M. Bukai, University of Twente, Faculty of Electrical Engineering, Mathematics, and Computer Science, Center for Telematics and Information Technology, The Netherlands. E-mail: e.m.bukai@utwente.nl.

David Wuthier, Luleå University of Technology, Department of Computer, Electrical and Space Engineering, Sweden. E-mail: david.wuthier@ltu.se.

George Nikolakopoulos, Luleå University of Technology, Department of Computer, Electrical and Space Engineering, Sweden. E-mail: geonik@ltu.se.

Stefano Stramigioli, University of Twente, Faculty of Electrical Engineering, Mathematics and Computer Science, Center for Telematics and Information Technology, The Netherlands. E-mail: s.stramigioli@utwente.nl.

Johan B.C. Engelen, University of Twente, Faculty of Electrical Engineering, Mathematics and Computer Science, Center for Telematics and Information Technology, The Netherlands. E-mail: j.b.c.engelen@utwente.nl.

Matteo Fumagalli, Aalborg University, Robotics, Vision and Machine Intelligence Laboratory, Department of Mechanical and Manufacturing Engineering, Copenhagen, Denmark. E-mail: m_fumagalli@m-tech.aau.dk.